

Flux coupled tunable superconducting resonator

Juliang Li,¹ Pete Barry,² Tom Cecil,¹ Marharyta Lisovenko,¹ Volodymyr Yefremenko,¹ Gensheng Wang,¹ Serhii Kruhlov,³ Goran Karapetrov,³ and Clarence Chang^{1,4,5}

¹Argonne National Laboratory, 9700 South Cass Ave., Lemont, IL, 60439, USA

²Cardiff University, Cardiff CF10 3AT, UK

³Department of Physics, Drexel University, 3141 Chestnut St., Philadelphia, PA 19104, USA

⁴University of Chicago, 5640 South Ellis Ave., Chicago, IL, 60637, USA

⁵Kavli Institute for Cosmological Physics, U. Chicago, 5640 South Ellis Ave., Chicago, IL, 60637, USA

(*Electronic mail: juliang.li@anl.gov)

We present a design and implementation of frequency-tunable superconducting resonator. The resonance frequency tunability is achieved by flux-coupling a superconducting LC-loop to a current-biased feedline; the resulting screening current leads to a change of the kinetic inductance and shift in the resonance frequency. The thin film aluminum resonator consists of an interdigitated capacitor and thin line inductors forming a closed superconducting loop. The magnetic flux from the nearby current feedline induces Meissner shielding currents in the resonator loop leading to change in the kinetic part of the total inductance of the resonator. We demonstrate continuous frequency tuning within 160 MHz around the resonant frequency of 2.7 GHz. We show that: (1) frequency upconversion is achieved when kHz AC modulation signal is superimposed onto the DC bias resulting in sidebands to the resonator tone; (2) three-wave mixing is attained by parametrically pumping the nonlinear kinetic inductance using a strong RF pump signal in the feedline. The simple architecture is amenable to large array multiplexing and on-chip integration with other circuit components. The concept could be applied in flux magnetometers, upconverters, and parametric amplifiers operating above 4 Kelvin cryogenic temperatures when alternative high critical temperature material with high kinetic inductance is used.

I. INTRODUCTION

With their high quality factors and easy planar fabrication, superconducting resonators have found wide use in applications such as astronomical detectors¹ and superconducting quantum computing^{2,3}. Tunable superconducting resonators are attractive as they provide an effective platform for interfacing with various forms of excitation including phonons^{4,5}, photons⁶⁻⁹ and electrical charges¹⁰ where fine frequency tuning is required to achieve desired coupling strength. They also have been developed for characterizing high kinetic inductance superconducting thin films¹¹.

Common approaches for realizing frequency-tunable microwave resonators include the use of Josephson junctions (JJ)¹²⁻¹⁷ and high kinetic-inductance superconducting wires¹⁸⁻²⁴. The high nonlinear inductance of Josephson junctions offers a large frequency tuning range. However, the junctions have relatively low saturation power due to their limited critical current. On the other hand, high kinetic inductance wires can be easily fabricated because of their simple geometries and are suitable for higher operating temperature and power arising from their higher critical temperature (T_c) and critical current (I_o) compared to JJs. Tuning the kinetic inductance requires DC current biasing the inductor, which has typically been realized through direct coupling of the bias current. Here, we present an architecture where this current couples through magnetic flux.

The paper is organized as follows: in Section II we discuss the operating principles and design of the resonator along with its fabrication process. Section III demonstrates flux coupling of both low frequency (~ 10 kHz) and high frequency (~ 5 GHz) AC signals which can be used for frequency upconversion and three-wave mixing processes. In section IV we describe operating the resonator as parametric amplifier

and demonstrating preliminary results showing gain for both degenerate and non-degenerate three-wave pumping. We conclude in Section V and discuss potential changes to the resonator to improve the frequency tunability and flux coupling strength.

II. RESONATOR DESIGN

Our tunable resonator design is illustrated in Fig. 1. Two inductors are placed in parallel with an interdigitated capacitor in the middle. The inductors and the two straight edges of the capacitor form a superconducting loop that can carry a continuous circulating Meissner current. Applying current to the readout line via DC ‘In’ and ‘Out’ ports generates a magnetic field and the corresponding total magnetic flux enclosed by the loop given by Eq. 1.

$$\Phi_{dc} = w \frac{\mu_0 I_{dc}}{2\pi} \log \left(\frac{r_2}{r_1} \right). \quad (1)$$

where I_{dc} is the DC current supplied through the readout line and Φ_{dc} is the resulting magnetic flux threading the superconducting loop. r_1 and r_2 (shown in Fig. 2) are the distances from the readout line to the two opposite edges of our square resonator loop that are parallel to the readout line, and w is the width of the square loop parallel to the readout line.

Flux quantization in the closed superconducting loop necessitates a circulating, or screening current (I_{sc}) given by

$$L_{\text{self}} \times I_{sc} + \Phi_{dc} = m\Phi_o, \quad (2)$$

where L_{self} is the self-inductance of the superconducting loop, Φ_o is the magnetic flux quantum, and m is integer of flux quanta present in the superconducting loop. This screening

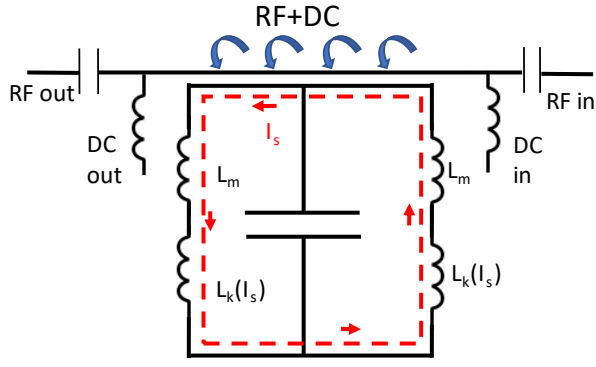


FIG. 1. Equivalent circuit of the flux biased tunable resonator. In the center is the interdigitated capacitor and the inductor carries both geometric (L_o) and kinetic (L_k) inductance. RF and DC currents are combined together through bias Tees and fed through the readout line. By Eq. 2, magnetic flux generated from DC current in the readout line (wide blue arrow bar) excites a screening current I_{sc} (red dash line) in the superconducting loop.

current will modify the kinetic inductance with relationship given by.

$$L_k \approx L_{k0} \left[1 + \left(\frac{I_{sc}}{I^*} \right)^2 \right], \quad (3)$$

where L_{k0} is the intrinsic kinetic inductance at zero current, and I^* sets the characteristic scale of the nonlinearity and has a value close to the superconducting critical current I_c ^{25,26}.

Starting from the design geometry of our resonator, we derive the relative frequency shift as a function of DC bias current I_{dc} as

$$\frac{\Delta f}{f_o} = \frac{\alpha(-MI_{dc} + m\Phi_0)^2}{2L_{self}^2 I^{*2}}, \quad (4)$$

where α is kinetic inductance participation ratio, M is the mutual inductance between the readout line and the superconducting loop. Details of the calculation could be found in Appendix A.

Fig. 2 shows the physical layout of the frequency tunable microwave resonator. The resonator consists of a central set of interdigitated fingers, which acts as the capacitor, and with both ends connected by narrow lines which act as inductors. The resonator is placed $2 \mu\text{m}$ away from a Nb microstrip readout line. The gap provides RF coupling to the feedline which is used for readout of the resonator via a microwave probe tone. Detailed parameters of the design can be found in Table I. Device fabrication is carried out using e-beam lithography and single-layer resist lift-off processes. The process begins with a low resistivity prime silicon wafer with native oxide. The wafer is coated with a 200 nm thick layer of PMMA 950 A4 resist. The resist is exposed in a JEOL JBX-8100FS e-beam writer at a dose of $720 \text{ mJ}/\text{cm}^2$ and developed in an MIBK and IPA mix (1:3). Next, a 30 nm thick Al layer is deposited via sputtering at a base pressure below 5×10^{-8} Torr. The wafer is then placed in Microposit 1165 remover to lift-off the residual Al stack. The readout line is

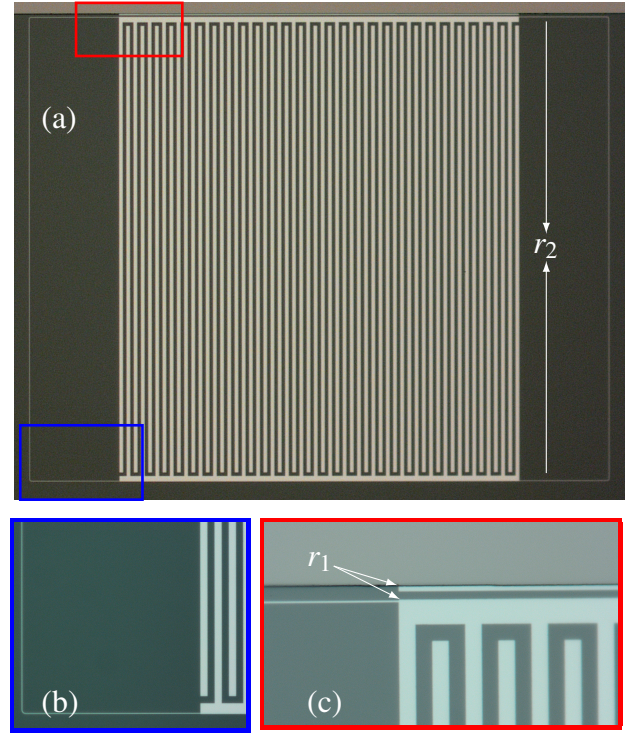


FIG. 2. **a**, image of the tunable resonator. Lighter color marks the Lumped LC resonator and the readout line that carries both the RF and DC signals. Darker color is the silicon substrate. In the center is the interdigitated capacitor and the narrow lines on both sides are the inductors. r_2 is the distance from the further end of the loop to the readout line that is used for flux calculation. **b**, zoom in image of the inductor with width of 400 nm and interdigitated capacitor in the blue rectangle of **a**. **c**, coupling of the LC resonator to the readout line corresponding to the area outlined by the red square of **a**. Darker color is the Nb readout line and the lighter color is part of the LC resonator. Q_c (coupling quality factor) for the resonator is determined by the gap between the resonator and the readout line, which we designed to be $2 \mu\text{m}$. r_1 is the distance from the closest end of the loop to the readout line that is used for flux calculation.

fabricated in a second step with the same lift-off process used on 300 nm of Nb. Two resonators are patterned with inductor widths of 400 nm and 300 nm and the same capacitor dimensions.

The resonator chip is measured in a dilution refrigerator with base temperature of 30 mK. The measured zero-bias resonant frequency for the two resonators, with inductor line width of 400 and 300 nm, are 3.148 and 2.705 GHz respectively. Fig. 3 shows the relative frequency shift $\Delta f/f_o = (f - f_o)/f_o$ for the two resonators as a function of applied DC current bias. Over 160 MHz frequency shift is observed for the 2.7 GHz resonator. Dashed lines show a fit to a polynomial relationship. Using Eq. 4 we calculate I^* to be 0.6 mA and 0.4 mA respectively for resonators with 400 nm and 300 nm inductors. These values are larger than values estimated through the measured critical current I_c (52 and 39 μA) and the assumption that $I^* \approx I_c$.

TABLE I. parameters of the flux biased resonator.

Capacitor:	
finger width (μm)	4
finger length (μm)	480
gap between fingers (μm)	4
gap between finger and capacitor end (μm)	4
number of finger pairs	28
length of capacitor end (μm)	500
width of capacitor end (μm)	6
Inductor:	
width (nm)	300, 400
length (μm)	700
f_o (GHz)	2.705, 3.148
Q_o (at $df/dI = 0$)	27,000, 90,000
Q_c (at $df/dI = 0$)	20,000, 15,000

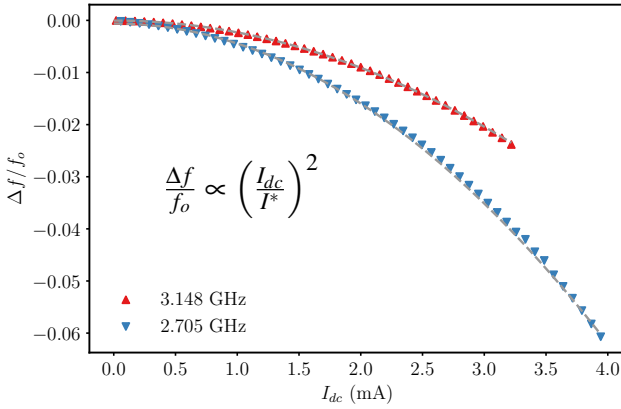


FIG. 3. Relative resonance shift $\Delta f/f_o$ as a function of DC bias current for the two Al resonators. The resonant frequency shifts to lower values with increasing biasing current following a parabolic relationship as expected from Eq. 4. Dashed lines are fits to a quadratic equation.

III. MIXING THROUGH FLUX BIASING

Our flux bias design also presents a mechanism for coupling AC signals. At lower frequencies, this attribute can be used to upconvert the signal. We can consider a low-frequency modulation at frequency ω_m with small amplitude I_m superimposed on top of a DC bias for a total current on the readout line $I'_{dc} = I_{dc} + I_m \sin(\omega_m t)$. Using Eq. A13 along with the first order Taylor expansion $(I_{dc} + I_m \sin(\omega_m t))^2 \approx I_{dc}^2 + 2I_{dc}I_m \sin(\omega_m t)$ for $I_m \ll I_{dc}$, we can write the resonant frequency as:

$$\omega'_o = \omega_o + \delta_{dc} + \delta_m, \quad (5)$$

where ω_o is the zero-bias resonant frequency, and

$$\delta_{dc} = -\frac{3\omega_o \alpha M^2 I_{dc}^2}{L_{\text{self}}^2 I_*^2}, \quad (6)$$

$$\delta_m = -6 \frac{d\omega}{dI_{dc}} I_m \sin(\omega_m t), \quad (7)$$

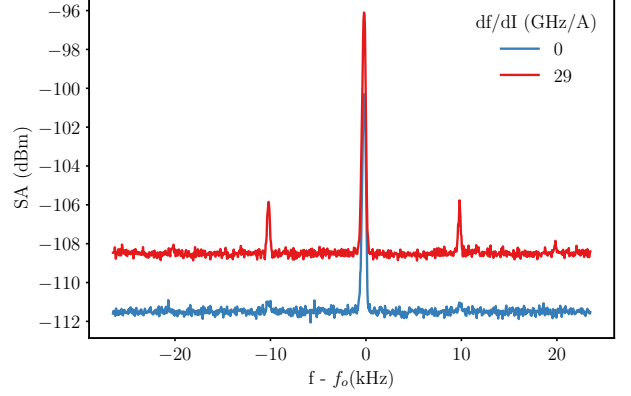


FIG. 4. Frequency upconversion of a 10kHz low frequency signal through a carrier tone at resonator frequency f_o . Without frequency detuning or current bias $df/dI_{dc} = 0$ minimum upconversion is observed above the noise floor of our measurement (blue curve). Applying a DC bias that shifts the resonance by 10MHz (corresponding to $df/dI_{dc} \neq 0$) we observe clear frequency upconversion as side bands around the center carrier peak (red curve).

correspond to the respective shifts in resonator frequency due to the DC bias and the modulation at ω_m . The response to the low frequency modulation, δ_m , is a modulation which appears in frequency domain as side bands at $\pm\omega_m$ on both sides of the resonator tone $\omega_o + \delta_{dc}$ with amplitude proportional to $d\omega/dI_{dc}$. We can demonstrate this upconversion empirically by applying a 10 kHz modulation on the bias line with and without a DC bias. We observe a prominent appearance of ± 10 kHz sidebands around the resonator frequency with the application of a DC bias (see Fig. 4) while keeping all other measurement parameters the same.

At higher frequencies, our flux coupling design can be utilized for parametric pumping through three-wave mixing^{27,28}. The system Hamiltonian under three-wave mixing is given by:

$$\begin{aligned} \mathcal{H} = & \hbar(\omega_o + \delta_{dc} + \delta_p + K - \frac{\omega_p}{2}) a^\dagger a \\ & + \frac{\hbar\xi}{2} a^{\dagger 2} + \frac{\hbar\xi^*}{2} a^2 + \frac{\hbar K}{2} a^{\dagger 2} a^2, \end{aligned} \quad (8)$$

with

$$\delta_p = -\frac{3\omega_o \alpha M^2 I_p^2}{4L_{\text{self}}^2 I_*^2}, \quad (9)$$

$$K = -\frac{3\hbar\omega_o^2 \alpha}{2L_T I_*^2}, \quad (10)$$

$$\xi = -\frac{3\omega_o \alpha M^2 I_{dc} I_p}{2L_{\text{self}}^2 I_*^2} e^{-i\phi_p}. \quad (11)$$

where we have used Eq. A9 to convert current in the loop (\bar{I}_{dc}) to bias current in the readout line (I_{dc}). ω_o is the zero-bias resonant frequency, L_T is the total inductance of the inductor which includes both geometric and kinetic inductance, δ_{dc} is same as in Eq. 6, δ_p is the resonance frequency shift from the pumping tone, K is the Kerr constant corresponding to

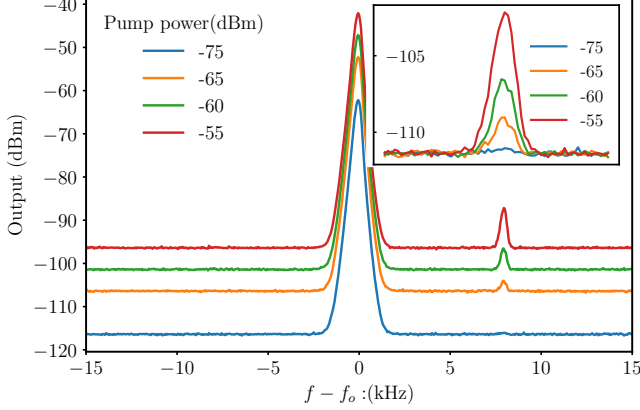


FIG. 5. measured three-wave mixing power spectrum. From bottom to top The curves correspond to monotonically increasing pump power. The curves are shifted vertically for better idler tone visibility. Pump power is calculated by subtracting the total lose in the input line from the output power of the signal generator. Both pump and signal generators as well spectrum analyzer are frequency locked through 10MHz reference ports. Inset is zoom in to the idler tone without vertical shift. Horizontal axis is frequency and vertical axis is power in dBm. Legend is pump power from -75 to -55 dBm the idler power increases from close to zero to 10 dB relative to the noise floor on the spectrum analyzer.

the nonlinearity of the system, ξ is the mixing strength under three-wave mixing and I_p is amplitude of the three-wave mixing tone ω_p (see Appendix C for detailed Hamiltonian construction).

We demonstrate the mixing process as follows: we apply a weak signal tone at frequency $\omega_s = \omega_o + \delta_{dc}$ and a strong pump tone at frequency $\omega_p = 2\omega_s + 8\text{kHz}$ to the readout line and measure the output signal with a spectrum analyzer. Three-wave mixing results in a signal at the idler frequency $\omega_i = \omega_s + 8\text{kHz}$, which appears as a side band at 8 kHz above the signal tone). Fig. 5 shows the results from our measurements with the curves, from bottom up, corresponding to increasing pump power with all other parameters kept constant. The curves have been shifted vertically for clarity. Inset is a zoom in at the idler tone showing that the power at the idler tone increases monotonically with the pump power, which is predicted by the dependence of the three-wave mixing rate ξ on the pump power I_p in Eq. 11.

We repeat this measurement by applying various DC biases which would also change the coupling strength. Results are shown in Fig. 6. From the system Hamiltonian, the strength of the three-wave mixing ξ increases linearly with DC current bias I_{dc} (Eq. 11). With each applied DC bias, we observe an expected shift in resonance frequency given by Eq. 9. We measured the idler sideband power for pump powers of -56 , -51 and -46 dBm at three DC biases corresponding to frequency detunings of (0, -5 and -10 MHz). At each detuning we linearly fit the sideband power to its pump power and observe that the slope of the fitted lines increases monotonically with detuning magnitude, which is consistent with the predicted increase in coupling strength.

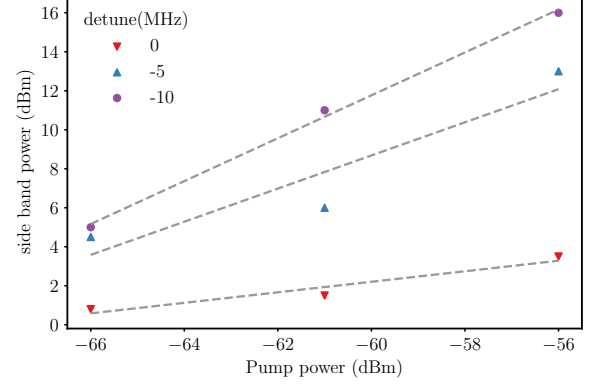


FIG. 6. Side band power as function of pump power for three different frequency detune or current bias point. In this power measurement we have deduced the noise floor of the spectrum analyzer from the peak power of the side bands.

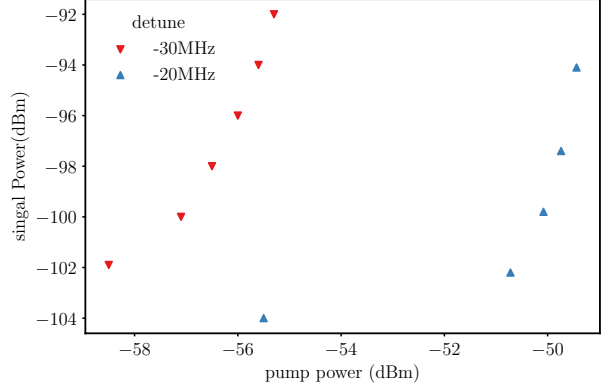


FIG. 7. Measured signal peak power under non-degenerate three-wave pumping as function of pump power at two frequency detuning points.

IV. DISCUSSION

Motivated by the above three-wave mixing result, we also qualitatively investigated the potential of the flux bias resonator to be used as a parametric amplifier. First, we operated the amplifier with non-degenerate three-wave pumping where the signal is detuned 4 kHz above resonant frequency and the pump is set at twice the resonant frequency. The signal peak power is measured with a spectrum analyzer. Fig. 7 shows the measured signal power as a function of pump power at two DC biases corresponding to two frequency detunings. The increased DC flux bias results in both larger detuning and a boost of the three-wave mixing strength ξ . Increasing the pump power eventually results in 10 dB gain on the signal for both detunings with the larger detuning showing amplification at lower pump amplitudes. This corresponds with the theoretical prediction that ξ is linearly proportional to both I_{dc} in the resonator as well as the pumping current amplitude I_p .

We also characterized the device gain under degenerate

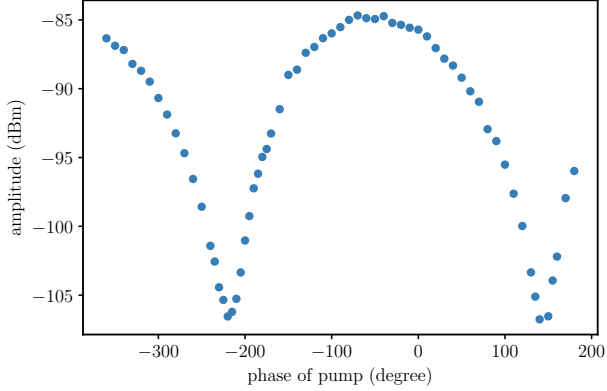


FIG. 8. Measured signal peak power under degenerate three-wave pumping as function of signal phase. Both pump power and phase as well as signal output power from generator remain constant during measurement while phase of the signal was changed by adjusting the phase parameter on the generator. Power of pump was set at -51dBm.

three-wave mixing, where a signal tone at the resonator frequency and a pump tone at twice the resonator frequency are applied. Under this condition the pump signal splits into pairs of signal and idler photons that are at the same frequency and the system gain varies with the phase difference between the pump and signal. Results of the measured signal peak as a function of the pump tone phase are shown in Fig. 8. Since the signal phase remains constant, changing the pump phase changes the relative phase between the pump and the signal and the measurement clearly demonstrates dependence of the amplification on the pump phase with a period of π . On the other hand, we varied the phase of the signal while keeping the pump phase constant and observed the expected change in amplification modulation period from π to $\pi/2$.

V. CONCLUSION

In conclusion, we have demonstrated the flux-bias tuning of the resonant frequency of a superconducting resonator by using the screening current induced by magnetic flux through a superconducting loop in combination with the non-linear inductance of a superconducting thin film. Our devices exhibits the expected frequency detuning as demonstrated by measurements of the frequency response for varying DC flux bias, along with the mixing of low frequency (\sim MHz) and high frequency (\sim GHz) signals. Our measurements also provides an initial demonstration of potential applications of this architecture including upconverting MHz signals and parametric amplification through three-wave mixing. Larger frequency detuning can potentially be achieved by fabricating devices with narrower and thinner loop wires and using other superconducting films such as Titanium nitride or Niobium nitride, which have very high kinetic inductance. Devices using these alternative materials may also enable operation at temperatures above 4 Kelvin.

DATA AVAILABILITY STATEMENT

Data used in this work is available on reasonable request.

ACKNOWLEDGEMENT

We thank Professor Jarryd Pla from UNSW of Sydney, Australia for very helpful discussion on system Hamiltonian construction. Work at Argonne National Lab, including work performed at the Center for Nanoscale Materials, a U.S. Department of Energy Office of Science User Facility, is supported by the U.S. Department of Energy, Office of Science, Office of High Energy Physics and Office of Basic Energy Sciences, under Contract No. DE-AC02-06CH11357. This material is based upon work supported by the U.S. Department of Energy Office of Science National Quantum Information Science Research Centers. The work at Q-Next includes concept development, design, fabrication, testing, and modeling of devices.

Appendix A: Calculation of $df/d\Phi$

Complete solution for self inductance of a rectangular loop is given as²⁹

$$L_{\text{self}} = \frac{\mu_o \mu_r}{\pi} \left[-2(w+h) + 2\sqrt{h^2+w^2} + \text{temp} \right] \quad (\text{A1})$$

with

$$\begin{aligned} \text{temp} = & -h \ln \left(\frac{h + \sqrt{h^2 + w^2}}{w} \right) - w \ln \left(\frac{w + \sqrt{h^2 + w^2}}{h} \right) \\ & + h \ln \left(\frac{2h}{d/2} \right) + w \ln \left(\frac{2w}{d/2} \right) \end{aligned}$$

TABLE II. mathematical symbols and corresponding definition

symbol	definition
ω_o	angular frequency of flux biased resonator
ω_m	angular frequency of modulation tone
L_k	kinetic inductance of Al inductor
$L_{k,o}$	intrinsic kinetic inductance of Al inductor
I_{sc}	screening current of superconducting loop
I^*	characteristic current of Al inductor
L_{self}	self inductance of superconducting loop
Φ_{dc}	external flux threading the superconducting loop
Φ_o	flux quantum
I_{dc}	DC bias current in the readout line
\bar{I}_{dc}	DC current in superconducting loop
\bar{I}_p	pump current in superconducting loop
L_o	geometric inductance of inductor
L_T	total inductance of inductor
α	kinetic inductance participation ratio
M	mutual inductance between readout line and loop
K	Kerr nonlinearity of the flux biased resonator
Q_o	internal quality factor
Q_c	external of coupling quality factor

where w, h are the width and height of the inductor square loop and d is the diameter of the inductor wire. We will ignore the small correction to this expression due to the presence of a ground plane³⁰.

The resonant frequency of an LC-resonator is given by:

$$f_t = \frac{1}{2\pi\sqrt{L_t C_t}} = \frac{1}{2\pi\sqrt{(L_o + L_{k,o} + \Delta L_k) C_t}} \quad (\text{A2})$$

$$= \frac{1}{2\pi\sqrt{(L_o + L_{k,o}) C_t}} \left(1 - \frac{\Delta L_k}{2(L_o + L_{k,o})} \right) \quad (\text{A3})$$

$$= f_o \left(1 - \frac{\Delta L_k}{2(L_o + L_{k,o})} \right) \quad (\text{A4})$$

with $f_o = 1/(2\pi\sqrt{(L_o + L_{k,o}) C_t})$ and $\Delta L_k = L_{k,o} (I_{sc}/I^*)^2$

The relative frequency shift due to change in kinetic inductance is expressed as:

$$\frac{\Delta f}{f_o} = \frac{f - f_o}{f_o} = \frac{-\Delta L_k}{2(L_o + L_{k,o})} \quad (\text{A5})$$

$$= \frac{L_{k,o}}{2(L_o + L_{k,o})} \left(\frac{I_{sc}}{I^*} \right)^2 \quad (\text{A6})$$

$$= \frac{L_{k,o}}{2(L_o + L_{k,o})} \left(\frac{I_{sc}}{I^*} \right)^2 \quad (\text{A7})$$

Expressing the screening current I_{sc} from Eq. 2

$$I_{sc} = \frac{-\Phi_{dc} + m\Phi_o}{L_{self}} \quad (\text{A8})$$

$$= \frac{-MI_{dc} + m\Phi_o}{L_{self}} \quad (\text{A9})$$

where M is the mutual inductance between the readout line and the superconducting loop. substituting I_{sc} into Eq. A9 we obtain:

$$\frac{\Delta f}{f_o} = \frac{L_{k,o}}{2L_{self}} \left(\frac{I_{sc}}{I^*} \right)^2 \quad (\text{A10})$$

$$= \frac{L_{k,o}(-MI_{dc} + m\Phi_o)^2}{2(L_o + L_{k,o})L_{self}^2 I^{*2}} \quad (\text{A11})$$

$$= \frac{\alpha(-MI_{dc} + m\Phi_o)^2}{2L_{self}^2 I^{*2}} \quad (\text{A12})$$

The derivative of frequency change versus current bias is:

$$\frac{df}{dI_{dc}} = \frac{f_o \alpha M^2}{L_{self}^2 I^{*2}} I_{dc} \quad (\text{A13})$$

where we have set the intrinsic loop flux $m = 0$.

Appendix B: optimization of $df/d\Phi$

several geometrical factors play a role in determining the relative magnitude of resonance frequency shift induced by the I_{DC} : the resonator geometry such as the width and length of the loop and the cross-section of the superconducting microstrip, as well as the mutual inductance between the resonator loop and the DC line. In our resonator design $Q_c \ll Q_o$

so the total quality factor Q_r is dominated by Q_c . We choose the width of the loop to be $500 \mu\text{m}$ because it gives us the high Q_c based on our related resonator design. It will be easier to achieve flux bias with a wider loop but at the same time Q_c will decrease. The gap between the resonator and the readout line is $2 \mu\text{m}$. A smaller gap will have more flux bias but it would also bring challenges related to lithographic patterning of the structure. At this point we prefer to limit ourselves with the best resolution of our optical lithography. Thus, in our designs we fixed the width to be $500 \mu\text{m}$ and gap to be $2 \mu\text{m}$.

In Fig. 9 we plot the df/dI_{dc} as a function of the loop height H from 0 to $10000 \mu\text{m}$ for loop microstrip diameter of $1 \mu\text{m}$ and the maximum frequency shift happens at $H \approx 200 \mu\text{m}$. This gives a guideline regarding the target parameters of the resonator design.

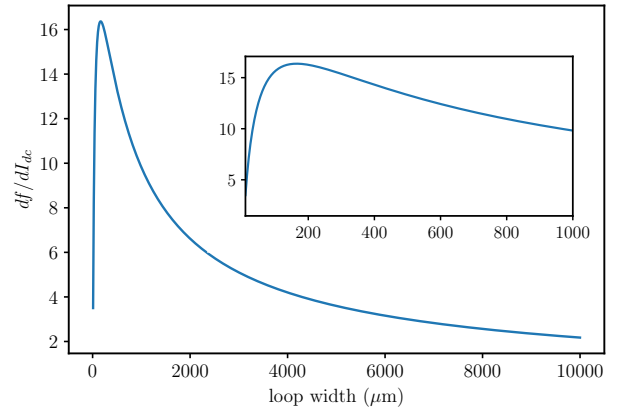


FIG. 9. $\partial f/\partial I_{dc}$ as a function of loop width W for loop strip of $1 \mu\text{m}$. Maximum happens at $W \approx 200 \mu\text{m}$. Inset is zoom in to the range of $1000 \mu\text{m}$ to show the maximum point.

Appendix C: nonlinear resonator model

For kinetic inductance based nonlinear resonator

$$L_k(I) = L_{k,o} \left(1 + \frac{I^2}{I^{*2}} \right) \quad (\text{C1})$$

calculated energy of the resonator is as follows:

$$U_C = \frac{1}{2} C \Phi^2 \quad (\text{C2})$$

$$U_L = \frac{1}{2} \frac{\Phi^2}{L_k + L_o} \quad (\text{C3})$$

$$= \frac{1}{2} \frac{\Phi^2}{L_{o,k} \left(1 + \frac{I^2}{I^{*2}} \right) + L_o} \quad (\text{C4})$$

$$= \frac{1}{2} \frac{\Phi^2}{L_T} - \frac{L_{o,k}}{2L_T^2} \frac{\Phi^4}{I^{*2}} \quad (\text{C5})$$

where $L_T = L_o + L_{k,o}$. L_o and $L_{k,o}$ is the geometric and kinetic inductance without current bias respectively. Lagrangian of

the resonator is given as

$$\mathcal{L} = U_C - U_L = \frac{1}{2}C\dot{\Phi}^2 - \frac{1}{2}L_T\Phi^2 + \frac{L_{o,k}}{2L_T^4 I^{*2}}\Phi^4 \quad (C6)$$

Using Legendre transformation $\mathcal{H} = \dot{\Phi}Q - \mathcal{L}$ the Hamiltonian is written as follows

$$\mathcal{H} = \frac{Q^2}{2C} + \frac{1}{2}L_T\Phi^2 - \frac{L_{o,k}}{2L_T^4 I^{*2}}\Phi^4 \quad (C7)$$

Replacing Q and Φ with their quantum operator the Hamiltonian now can be written as

$$\tilde{\mathcal{H}} = \frac{\tilde{Q}^2}{2C} + \frac{1}{2}L_T\tilde{\Phi}^2 - \frac{L_{o,k}}{2L_T^4 I^{*2}}\tilde{\Phi}^4 \quad (C8)$$

we can further separate the Hamiltonian into its linear $\tilde{\mathcal{H}}_o$ and interaction $\tilde{\mathcal{H}}_1$ part

$$\tilde{\mathcal{H}}_o = \frac{\tilde{Q}^2}{2C} + \frac{1}{2}L_T\tilde{\Phi}^2 \quad (C9)$$

$$\tilde{\mathcal{H}}_1 = -\frac{L_{o,k}}{2L_T^4 I^{*2}}\tilde{\Phi}^4 \quad (C10)$$

Defining the following creation and annihilation operators

with $\omega_o = 1/\sqrt{L_T C}$

$$\tilde{a} = \frac{1}{\sqrt{\hbar\omega_o}} \left[\frac{1}{\sqrt{2L_T}}\tilde{\Phi} + i\frac{1}{\sqrt{2C}}\tilde{Q} \right] \quad (C11)$$

$$\tilde{a}^\dagger = \frac{1}{\sqrt{\hbar\omega_o}} \left[\frac{1}{\sqrt{2L_T}}\tilde{\Phi} - i\frac{1}{\sqrt{2C}}\tilde{Q} \right] \quad (C12)$$

the reduced flux operator in terms of \tilde{a} and \tilde{a}^\dagger

$$\tilde{\Phi} = \sqrt{\hbar\omega_o L_T/2}(\tilde{a}^\dagger + \tilde{a}) \quad (C13)$$

and the interaction Hamiltonian is

$$\tilde{\mathcal{H}}_1 = -\frac{L_{o,k}}{2L_T^4 I^{*2}}(\hbar\omega_o L_T/2)^2(\tilde{a}^\dagger + \tilde{a})^4 \quad (C14)$$

$$= -\frac{3L_{o,k}(\hbar\omega_o L_T)^2}{4L_T^4 I^{*2}}(2\tilde{a}^\dagger\tilde{a} + \tilde{a}^{\dagger 2}\tilde{a}^2) \quad (C15)$$

$$= \hbar K\tilde{a}^\dagger\tilde{a} + \frac{1}{2}\hbar K\tilde{a}^{\dagger 2}\tilde{a}^2 \quad (C16)$$

and $K = -\frac{3\hbar\omega_o^2 L_{o,k}}{2L_T^4 I^{*2}} = -\frac{3\hbar\omega_o^2 \alpha}{2L_T I^{*2}}$. α is the participation ratio of the kinetic inductance

with DC bias \bar{I}_{dc} and parametric pump mode \bar{I}_p in the resonator

$$\mathcal{H}_1 = \frac{1}{2}\hbar K(2a^\dagger a + a^{\dagger 2}a^2) - \frac{L_{o,k}}{2L_T^4 I^{*2}}6(\hbar\omega_o L_T/2)L_T^2 [\bar{I}_{dc}^2 + 2\bar{I}_{dc}\bar{I}_p(t) + \bar{I}_p^2(t)](2a^\dagger a + a^{\dagger 2} + a^2) \quad (C17)$$

$$= \frac{1}{2}\hbar K(2a^\dagger a + a^{\dagger 2}a^2) - \frac{3\hbar\omega_o \alpha}{2I^{*2}}[\bar{I}_{dc}^2 + 2\bar{I}_{dc}\bar{I}_p(t) + \bar{I}_p^2(t)](2a^\dagger a + a^{\dagger 2} + a^2) \quad (C18)$$

the time dependent pump mode can be written as

$$\bar{I}_p(t) = \frac{\bar{I}_p}{2} \left(e^{-i(\omega_p t + \phi_p)} + e^{i(\omega_p t + \phi_p)} \right) \quad (C19)$$

Apply rotating wave approximation (RWA)

$$\mathcal{H}'_1 = U^\dagger \mathcal{H}_1 U - i\hbar U^\dagger \frac{\partial}{\partial t} U \quad (C20)$$

and

$$U^\dagger = \exp(i\omega_p t a^\dagger a/2) \quad (C21)$$

$$U = \exp(-i\omega_p t a^\dagger a/2) \quad (C22)$$

We transfer the Hamiltonian into frame rotating at $\omega_p/2$

$$\mathcal{H} = \hbar(\omega_o + \delta_{dc} + \delta_p + K - \frac{\omega_p}{2})a^\dagger a \quad (C23)$$

$$+ \frac{\hbar\xi}{2}a^{\dagger 2} + \frac{\hbar\xi^*}{2}a^2 + \frac{\hbar K}{2}a^{\dagger 2}a^2 \quad (C24)$$

$$\delta_{dc} = -\frac{3\omega_o \alpha \bar{I}_{dc}^2}{I^{*2}} \quad (C25)$$

$$\delta_p = -\frac{3\omega_o \alpha \bar{I}_p^2}{4I^{*2}} \quad (C26)$$

$$K = -\frac{3\hbar\omega_o^2 \alpha}{2L_T I^{*2}} \quad (C27)$$

$$\xi = -\frac{3\omega_o \alpha \bar{I}_{dc} \bar{I}_p}{2I^{*2}} e^{-i\phi_p} \quad (C28)$$

the system Hamiltonian can be calculated by setting the pump amplitude to zero and

$$\mathcal{H} = \hbar(\omega_o + \delta_{dc} + K)a^\dagger a + \frac{\hbar K}{2}a^{\dagger 2}a^2 \quad (C29)$$

$$\delta_{dc} = -\frac{3\omega_o \alpha \bar{I}_{dc}^2}{I^{*2}} \quad (C30)$$

¹P. K. Day, H. G. LeDuc, B. A. Mazin, A. Vayonakis, and J. Zmuidzinas, "A broadband superconducting detector suitable for use in large arrays," Nature **425**, 817–821 (2003).

- ²A. Wallraff, D. I. Schuster, A. Blais, L. Frunzio, R.-S. Huang, J. Majer, S. Kumar, S. M. Girvin, and R. J. Schoelkopf, “Strong coupling of a single photon to a superconducting qubit using circuit quantum electrodynamics,” *Nature* **431**, 162–167 (2004).
- ³A. Blais, R.-S. Huang, A. Wallraff, S. M. Girvin, and R. J. Schoelkopf, “Cavity quantum electrodynamics for superconducting electrical circuits: An architecture for quantum computation,” *Phys. Rev. A* **69**, 062320 (2004).
- ⁴J. D. Teufel, D. Li, M. S. Allman, K. Cicak, A. J. Sirois, J. D. Whittaker, and R. W. Simmonds, “Circuit cavity electromechanics in the strong-coupling regime,” *Nature* **471**, 204–208 (2011).
- ⁵X. Han, C.-L. Zou, and H. X. Tang, “Multimode strong coupling in superconducting cavity piezoelectromechanics,” *Phys. Rev. Lett.* **117**, 123603 (2016).
- ⁶J. Bochmann, A. Vainsencher, D. D. Awschalom, and A. N. Cleland, “Nanomechanical coupling between microwave and optical photons,” *Nature Physics* **9**, 712–716 (2013).
- ⁷K. C. Balram, M. I. Davanço, J. D. Song, and K. Srinivasan, “Coherent coupling between radiofrequency, optical and acoustic waves in piezo-optomechanical circuits,” *Nature Photonics* **10**, 346–352 (2016).
- ⁸S. Barzanjeh, M. Abdi, G. J. Milburn, P. Tombesi, and D. Vitali, “Reversible optical-to-microwave quantum interface,” *Phys. Rev. Lett.* **109**, 130503 (2012).
- ⁹R. W. Andrews, R. W. Peterson, T. P. Purdy, K. Cicak, R. W. Simmonds, C. A. Regal, and K. W. Lehnert, “Bidirectional and efficient conversion between microwave and optical light,” *Nature Physics* **10**, 321–326 (2014).
- ¹⁰B. Brock, J. Li, S. Kanhirathingal, B. Thyagarajan, M. Blencowe, and A. Rimberg, “Fast and ultrasensitive electrometer operating at the single-photon level,” *Phys. Rev. Appl.* **16**, L051004 (2021).
- ¹¹D. Das, A. Naji, K. K. S. Multani, A. H. Safavi-Naeini, and E. A. Nanni, “Superconducting on-chip tunable mm-wave resonator,” in *2022 47th International Conference on Infrared, Millimeter and Terahertz Waves (IRMMW-THz)* (2022) pp. 1–2.
- ¹²M. Sandberg, C. M. Wilson, F. Persson, T. Bauch, G. Johansson, V. Shumeiko, T. Duty, and P. Delsing, “Tuning the field in a microwave resonator faster than the photon lifetime,” *Applied Physics Letters* **92**, 203501 (2008), <https://doi.org/10.1063/1.2929367>.
- ¹³Z. L. Wang, Y. P. Zhong, L. J. He, H. Wang, J. M. Martinis, A. N. Cleland, and Q. W. Xie, “Quantum state characterization of a fast tunable superconducting resonator,” *Applied Physics Letters* **102**, 163503 (2013), <https://doi.org/10.1063/1.4802893>.
- ¹⁴B. Abdo, A. Kamal, and M. Devoret, “Nondegenerate three-wave mixing with the josephson ring modulator,” *Phys. Rev. B* **87**, 014508 (2013).
- ¹⁵M. A. Castellanos-Beltran and K. W. Lehnert, “Widely tunable parametric amplifier based on a superconducting quantum interference device array resonator,” *Applied Physics Letters* **91**, 083509 (2007), <https://doi.org/10.1063/1.2773988>.
- ¹⁶K. D. Osborn, J. A. Strong, A. J. Sirois, and R. W. Simmonds, “Frequency-tunable josephson junction resonator for quantum computing,” *IEEE Transactions on Applied Superconductivity* **17**, 166–168 (2007).
- ¹⁷A. Palacios-Laloy, F. Nguyen, F. Mallet, P. Bertet, D. Vion, and D. Esteve, “Tunable resonators for quantum circuits,” *Journal of Low Temperature Physics* **151**, 1034–1042 (2008).
- ¹⁸M. Xu, X. Han, W. Fu, C.-L. Zou, and H. X. Tang, “Frequency-tunable high-q superconducting resonators via wireless control of nonlinear kinetic inductance,” *Applied Physics Letters* **114**, 192601 (2019), <https://doi.org/10.1063/1.5098466>.
- ¹⁹J. E. Healey, T. Lindström, M. S. Colclough, C. M. Muirhead, and A. Y. Tzalenchuk, “Magnetic field tuning of coplanar waveguide resonators,” *Applied Physics Letters* **93**, 043513 (2008), <https://doi.org/10.1063/1.2959824>.
- ²⁰M. R. Vissers, J. Hubmayr, M. Sandberg, S. Chaudhuri, C. Bockstiegel, and J. Gao, “Frequency-tunable superconducting resonators via nonlinear kinetic inductance,” *Applied Physics Letters* **107**, 062601 (2015), <https://doi.org/10.1063/1.4927444>.
- ²¹N. Samkharadze, A. Bruno, P. Scarlino, G. Zheng, D. P. DiVincenzo, L. DiCarlo, and L. M. K. Vandersypen, “High-kinetic-inductance superconducting nanowire resonators for circuit qed in a magnetic field,” *Phys. Rev. Appl.* **5**, 044004 (2016).
- ²²A. Kher, P. K. Day, B. H. Eom, J. Zmuidzinas, and H. G. Leduc, “Kinetic inductance parametric up-converter,” *Journal of Low Temperature Physics* **184**, 480–485 (2016).
- ²³A. A. Adamyany, S. E. Kubatkin, and A. V. Danilov, “Tunable superconducting microstrip resonators,” *Applied Physics Letters* **108**, 172601 (2016), <https://doi.org/10.1063/1.4947579>.
- ²⁴J. Luomahaara, V. Vesterinen, L. Grönberg, and J. Hassel, “Kinetic inductance magnetometer,” *Nature Communications* **5**, 4872 (2014).
- ²⁵S. Anlage, H. Snortland, and M. Beasley, “A current controlled variable delay superconducting transmission line,” *IEEE Transactions on Magnetics* **25**, 1388–1391 (1989).
- ²⁶A. J. Annunziata, *Single-Photon Detection, Kinetic Inductance, and Non-Equilibrium Dynamics in Niobium and Niobium Nitride Superconducting Nanowires*, Ph.D. thesis, Yale University, Connecticut (2010).
- ²⁷C. Macklin, K. O’Brien, D. Hover, M. E. Schwartz, V. Bolkhovskoy, X. Zhang, W. D. Oliver, and I. Siddiqi, “A near-quantum-limited josephson traveling-wave parametric amplifier,” *Science* **350**, 307–310 (2015), <https://www.science.org/doi/pdf/10.1126/science.aaa8525>.
- ²⁸D. J. Parker, M. Savvitskiy, W. Vine, A. Laucht, T. Duty, A. Morello, A. L. Grimsmo, and J. J. Pla, “Degenerate parametric amplification via three-wave mixing using kinetic inductance,” *Phys. Rev. Appl.* **17**, 034064 (2022).
- ²⁹C. R. Paul, *Inductance: Loop and Partial* (Wiley-IEEE Press, 2009).
- ³⁰X. Jia, L. Liu, and G. Fang, “The finite-conducting ground’s effect on the inductance of a rectangular loop,” *Journal of Sensors* **2016** (2015), 10.1155/2016/2765812.